Materials Science & Engineering A 766 (2019) 138368

Contents lists available at ScienceDirect

Materials Science & Engineering A

journal homepage: www.elsevier.com/locate/msea

Microstructure and mechanical properties of dissimilar friction stir welded AA2024-7075 joints: Influence of joining material direction

Chenghang Zhang[a], Guangjie Huang[a,*], Yu Cao[a,**], Yulong Zhu[a], Wei Li[a], Xiaodong Wang[b], Qing Liu[a]

[a] School of Materials Science and Engineering, Chongqing University, Chongqing, 400044, China
[b] Henan Engineering Research Center for Wear of Material, Luoyang, 471023, China

ARTICLE INFO

Keywords:
Aluminum alloys
Friction stir welding
Material flow
Texture
Mechanical properties

ABSTRACT

In order to assess the influence of joining material direction on the microstructure and mechanical properties of dissimilar friction stir welded joints, AA2024-T351 and AA7075-T651 sheets were joined with six different types of combination: RD‖RD, TD‖TD, RD‖TD, 45°‖45°, 45°‖RD and TD‖45° (RD, TD and 45° mean the rolling direction, transverse direction, 45° to the rolling direction, respectively). The results show that various types of welding combinations with respect to joining material direction affect the mechanical properties of joints due to the variations of material flow behavior and microstructure. Material mixed flow mainly occurs at three different regions, namely the tool shoulder domain, the tool pin domain and the transition region between them. The tunnel defect resulting from the insufficient heat input is generated with the combination type of 45°‖RD, resulting in the deteriorated tensile properties, while sound joints can be achieved through the other five types of combinations. The maximum tensile strength is acquired as 445.6 MPa for the RD‖TD joint as a result of suitable heat input and sufficient material flow. In the NZ, the average grain size in the center zone is higher than that in the bottom zone. The center interface zone of all the six joints contains B and $\overline{B}$ texture components, and C texture also appears in central interface zone of the TD‖TD and 45°‖RD joints. A_1^* and A_2^* texture components can be found in the bottom interface zone of all the six joints.

1. Introduction

Many special properties of aluminum alloys, such as light weight and excellent structural strength, capacitate them to be used for producing the structural parts [1,2]. High strength aluminum alloys, i.e., 2xxx and 7xxx series, are extensively employed for aircraft structures and other structural applications [3], especially for the dissimilar welding of these two alloys [4]. The structural parts and frames comprised of these aluminum alloys can be welded by using conventional fusion welding, which also leads to numerous defects including porosity, distortion, hot cracking and precipitates dissolution in the dissimilar joints [5]. As a promising solid-state welding, friction stir welding (FSW), as a method to join 2xxx and 7xxx series high strength aluminum alloys, has various advantages over traditional fusion welding [6,7]. Since the temperature produced by FSW is lower than the melting point of the materials being welded [8], some defects such as brittle inter dendritic and eutectic phases generated during solidification can be eliminated [9]. Accordingly, the FSW technology is being emphasized by the modern aerospace industry for its underlying high performance structural applications [10]. It can also be employed to assemble dissimilar materials which become more and more crucial in a large number of industrial sectors because of technical and economic benefits of dissimilar materials joints [6].

Many previous investigations about FSW based on experiments and simulations are primarily concentrated on the effect of process parameters [6,11–13] (tool geometry, rotational speed, welding speed, tool angle, backing material and clamping system, base materials and their arrangement in the advancing side (AS) or retreating side (RS), base material thickness) on the performance and quality of welding. Park et al. [14] investigated the influence of material locations on the properties of 2 mm thick AA5052-H32 and AA6061-T6 joints. They found that material mixing patterns depend mainly on the positions of base materials (BMs) and the stir zone is more adequately mixed when AA5052-H32 is located in the AS. Cavaliere et al. [15] and Palanivel et al. [16] revealed that when FSW line is parallel to the rolling direction (RD) of materials on the AS and perpendicular to the RD of

* Corresponding author.
** Corresponding author.
E-mail addresses: gjhuang@cqu.edu.cn (G. Huang), yucao928@cqu.edu.cn (Y. Cao).

https://doi.org/10.1016/j.msea.2019.138368
Received 31 March 2019; Received in revised form 15 August 2019; Accepted 31 August 2019
Available online 03 September 2019
0921-5093/

materials on the RS, this assembly type of joint can simulate the most severe mechanical combination with respect to the conventional reference welding trials. Kim et al. [17] conducted three types of weld combinations with respect to the joining material direction and found that strength and ductility of the FSW AA6111-T4 joints with 1.5 mm thickness can be slightly improved with the combination type of RD‖RD, TD‖RD, TD‖TD (TD means the transverse direction). However, the types of welding combinations for the joints are less considered when the FSW joints are subjected to the forces from different directions under the actual working conditions. In addition, there have been few works concerning the microstructure evolution in the joints. Barbini et al. [18] examined the influence of material position, rolling and welding directions on properties of the dissimilar FSW AA2024-7050 joints and then proposed that the different material positions have a significant effect on the material transportation and the interface in the NZ. They also observed that the mechanical performance increases when the lower strength alloy is located on the AS. But the microstructure analysis of the weld zone in the joints are still lacking. The relationship between microstructure and mechanical properties has been rarely described. Based on the above researches, it can be concluded that different combinations types of BMs significantly influence the microstructure and properties of the FSW joints. However, there is extremely limited information available on the effect of BMs rolling direction on the microstructure and mechanical properties of dissimilar FSW joints.

In this investigation, we systematically studied the influence of rolling direction of BMs on the microstructure, material flow behavior and mechanical properties of dissimilar FSW joints of AA2024-T351 and AA7075-T651. The dissimilar FSW joints were produced with six different types of combinations: RD‖RD, TD‖TD, RD‖TD, 45°‖45°, 45°‖RD and TD‖45°. Material flow behavior in the nugget zone (NZ) was investigated in detail. The grain structure and texture in the center and bottom interface zone of the NZ was also analyzed. The hardness and tensile tests were conducted to evaluate the mechanical properties of different welded joints.

2. Experimental procedure

Aluminum alloy sheets AA2024-T351 and AA7075-T651 with thickness of 5 mm were butt-welded by FSW machine (FSW-LM-AM16-2D) under the rotational speed of 1050 rev/min and the welding speed of 170 mm/min. The chemical composition and mechanical properties of the two BMs are shown in Tables 1 and 2. The weld configuration arranges the AA2024 on the AS and the AA7075 on the RS (2A7R), as indicated in Fig. 1a. The reasons for choosing this type of welding are as follows. First, according to our previous tensile experiment results, the tensile strength of the 2A7R joints is relatively higher than that of the 7A2R joints at different rotational speeds. Second, it can be observed that the AA7075 is characterized by light colors, while AA2024 is featured with dark colors through metallography due to their different etching responses to the Keller's reagent. The materials from the AS occupy the majority zone of the NZ. If the AA2024 zone in the NZ of the 2A7R joints is just corroded, the AA7075 zone subjected to a slight corrosion is visible through the metallographic observation. However, if the AA7075 zone in the NZ of the 7A2R joints has been already corroded, AA2024 zone should be deeply corroded, which can not be observed from the metallographic images. Therefore, we determined that to place AA2024 on the AS is a better choice to analyze the microstructure of the NZ.

Table 1
Chemical composition of the aluminum alloys (in wt.%).

	Si	Fe	Cu	Mn	Mg	Cr	Zn	Ti	Al
2024-T351	0.05	0.17	4.5	0.6	1.4	0.01	0.03	0.02	Bal.
7075-T651	0.05	0.19	1.7	0.04	2.4	0.2	5.8	0.03	Bal.

Table 2
Mechanical properties of the aluminum alloys.

	Yield strength (YS, MPa)	Ultimate tensile strength (UTS, MPa)	Tensile elongation (TE, %)
2024-T351	360	470	20.3
7075-T651	476	555	11.4

The dissimilar FSW joints with respect to base material rolling directional combinations were joined with six different types of combinations: RD‖RD, TD‖TD, RD‖TD, 45°‖45°, 45°‖RD and TD‖45° (45° means 45° to the RD), as portrayed in Fig. 1b. The welding tool was characterized by a tapered thread probe with 3.8 mm in tip diameter and 5 mm in length, as well as a concave shoulder of 15 mm in diameter. The tilting angles of the probe were kept constant at 2.5° from the normal direction (ND) of work sheets towards the trailing side of the tool.

The welded samples were transversely sectioned and polished up to 3000 grit SiC papers followed by cloth polishing using diamond abrasion paste of 0.5 and 0.25 μm, respectively. The polished samples were finally etched with a Keller reagent (5 ml HNO_3, 2 ml HF, 3 ml HCl, 190 ml H_2O) during 40 s to carry out the optical microscopy (OM) tests. The distribution of the second phase particles and alloy elements in the NZ was observed by using field emission scanning electron microscopy (FESEM, JEOL JSM-7800F) equipped with an energy dispersive spectroscopy (EDS). The electron backscatter diffraction (EBSD) mapping was performed on a TESCAN MIRA3 SEM equipped with a HKL-EBSD system using a step size of 0.3 μm to study the grain microstructure. Before EBSD, the EBSD samples were electropolished in an electrolyte of 10 vol% perchloric acid plus 90 vol% ethanol at 2–5 °C and 15 V for 100 s. All EBSD data were analyzed using the Channel 5 software. A transmission electron microscope (TEM, FEI TECNAI G2 F20) was used to acquire information on the state of precipitated phases, which was operated at 200 kV. The TEM specimens were ground to 60 μm and rushed into 3 mm in diameter, and then they were prepared in a 25% HNO_3 methanol solution at −30 °C using the twin-jet electropolishing technique.

As illustrated in Fig. 1a, tensile samples were cut with a 40 mm gauge length and 4 mm width from the transverse section of weld region perpendicular to the welding direction (WD) and then tested using a Shimadzu AG-X plus universal testing machine at a crosshead speed of 1 mm/min. The size of the clamping end at both ends of the tensile samples should not be too small, or the clamping end may slip easily during the tensile test. Thus the welded zone has been completely covered by using the gauge of 40 mm and the fracture position of the joints can be more intuitively analyzed. Three tensile samples were prepared from each joint. Three-dimensional (3D) micro-hardness distribution was acquired across the whole weld region on the polished cross-sections under a load of 200 g for 10 s. A total of five test lines were measured across the weld at intervals of 1 mm, with a total of 265 indentations.

3. Results and discussion

3.1. Material flow and mixing

Fig. 2 shows the macrostructures of cross-sections of the joints obtained in six types of weld combinations. Three samples were taken at different positions of each joint. Evidently, it is observed that the NZ of the six kinds of joints presents an asymmetrical basin shape on the whole, but there are still some differences in the local area. One can clearly find that all the joints have no defects or any other imperfection except the v joint, in which a typical tunnel defect exists. Two welding experiments were conducted to confirm that this type of defect is

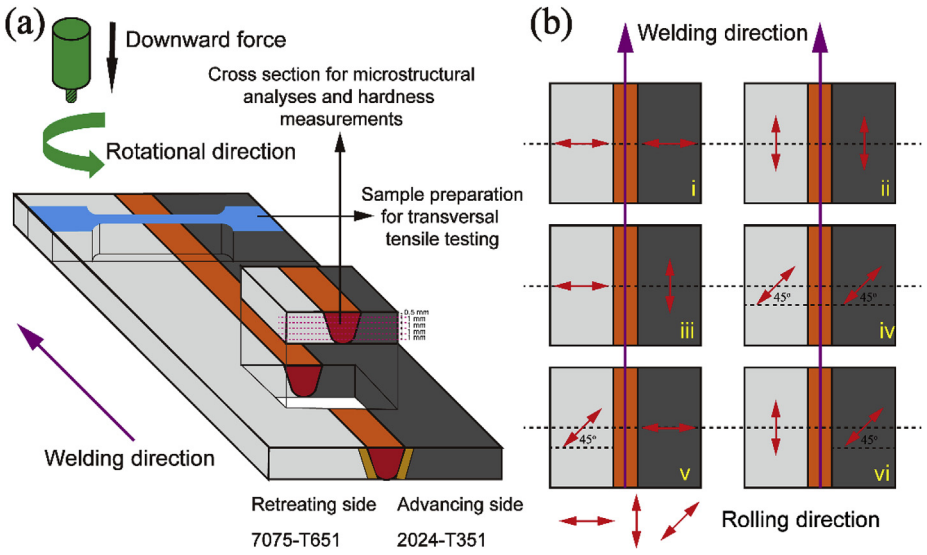

Fig. 1. Schematic view of FSW processing (a) the specimens of joints, (b) Weld combinations: (i) RD‖RD, (ii) TD‖TD, (iii) RD‖TD, (iv) 45°‖45°, (v) 45°‖RD and (vi) TD‖45°.

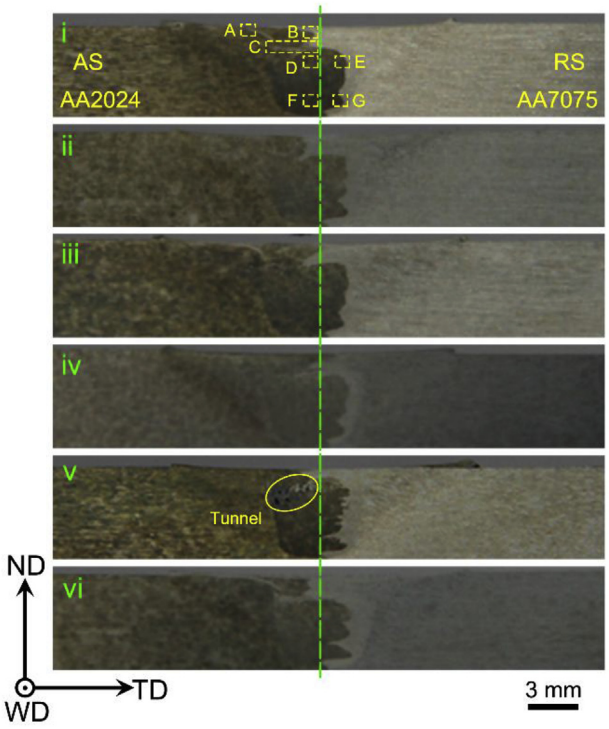

Fig. 2. Cross-sectional morphology of the six different combination types of the FSW joints.

systematically produced in the v joint. This is because three metallographic samples were taken for observation and tunnel defect was observed in all the three samples after each welding test. Tunnel defect is a common defect during FSW, which greatly affects the mechanical properties of the joints. It is sometimes referred to as wormhole because they are similar in appearance. Normally, it is not visible on the surface as it is formed inside the weld and below the surface of the weld. It has been reported that low heat input leads to the formation of tunnel defect [19]. Lower heat input causes higher flow stress, resulting in more insufficient material movement which hinders material mixing or coalition [20]. Therefore, this implies that the welding combination type of 45°‖RD produces a lower heat input, which results in insufficient plasticization of the materials and unbalance in material flow around tool pin, and in turn causes the tunneling defect.

Compared with the cross-sectional morphologies of the six joints in Fig. 1, material mixing in the local area of the NZ can be more clearly observed because the two BMs display significantly different contrast under the BSE signal. As illustrated in Fig. 3, a wider top and a narrower bottom present in the NZ due to the influence of the shape of the stirring tool. All the joints show a tendency for material flowing from the AS to the RS. The severely deformed NZ appears to be made up of these two BMs, and the AA2024 BM on the AS occupies most of the NZ.

In addition, the boundary between the NZ and the TMAZ on the AS is more salient than that on the RS. This is in connection with plastic deformation in the welding process [21]. During FSW, a non-consumable rotating tool stiffer than the BMs is inserted into the adjacent edges of the plates through sufficient axial force and moves along the welding direction. The friction heat generated by the tool shoulder and pin softens the materials around the pin. The softened materials are pushed to the forward direction under the action of tool movement. At this time, the shoulder prevents the plastically deformed materials from being extruded out of the weld. The plasticized AA2024 BM on the AS is shoved to the back of the pin. Moreover, the linear speed of the AA2024 BM on the AS is equal to the sum of the rotational speed and the welding speed, while the deformation direction of the AA7075 BM on the RS is the difference between of them. As a consequence, the boundary of the TMAZ on the AS is conspicuous, while the tendency of gradual transition presents in the boundary between the NZ and the TMAZ on the RS due to more uniform temperature distribution.

Based on the flow patterns in the NZ of the joints in Fig. 3, the NZ can be divided into two main areas namely the shoulder domain and the pin domain. Flow arm appears in the shoulder area near the AS direction, which indicates that material flow mixing behavior occurs in the shoulder area.

Fig. 4 displays the optical micrographs of A, B, E and G regions in the six different combination types of the joints in Fig. 2. The flow arm mainly appears in the A region and is characterized by the alternating distribution of the two BMs. The B region is the interface area where AA2024 BM on the AS flows to the RS direction. It is visible from Fig. 4 that different flow trace patterns present in the B region of all the joints. In the shoulder domain (A and B regions in Fig. 4), AA7075 on the RS is pushed to the AS direction. Meanwhile, AA2024 BM on the AS flows towards the RS direction under the extrusion and rotation of the tool. E and G regions in Fig. 4 are the interface areas where material flow, which are affected by the action of the root and tip of the tool pin. Compared to the A, B, E and G regions in the six joints, the material mixing of the iii joint is most apparent because more 2024 BM moves further to the RS, while the v joint is the worst due to obvious flow

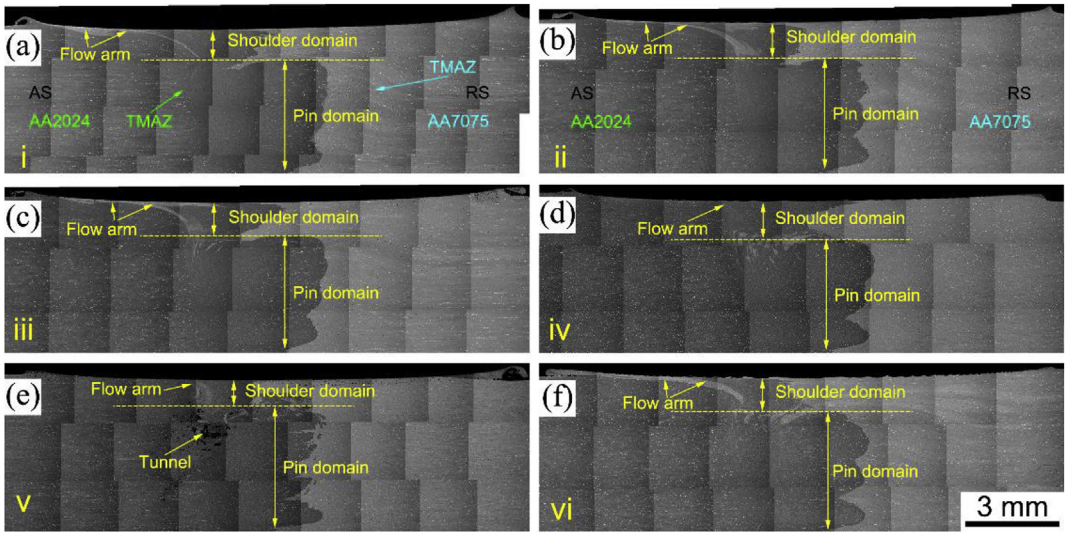

Fig. 3. BSE image puzzles of the six different combination types of the joints in Fig. 2.

traces at the interface in E and G regions.

The BSE images and the metallographic puzzles of the C region between the shoulder domain and the pin domain in the six joints are exhibited in Figs. 5 and 6, respectively. Clearly, there is an obvious hybrid trajectory of material flow in the C region. The rotation and movement of the tool pin break up the interfaces of the two BMs and redistribute the two alloys during welding process, which are mixed together by alternate distribution composing of AA2024 and AA7075

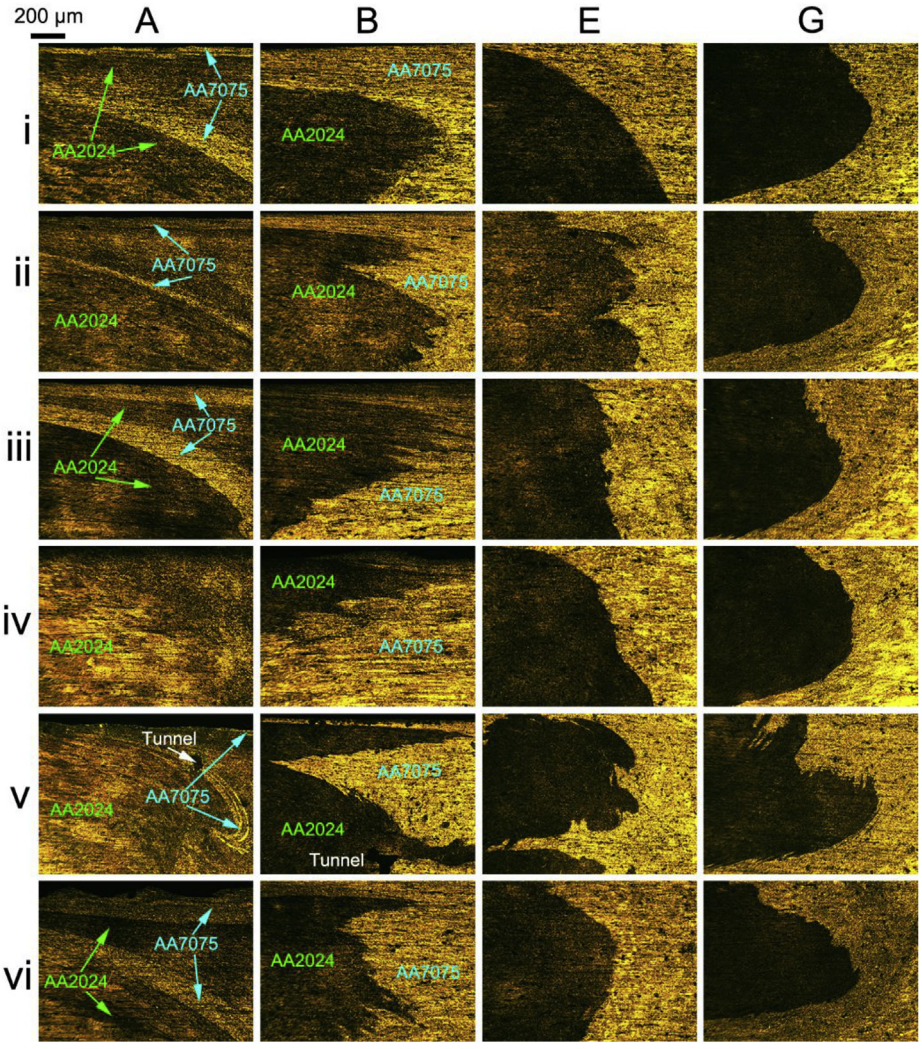

Fig. 4. Optical micrographs of A, B, E and G regions in the six joints in Fig. 2.

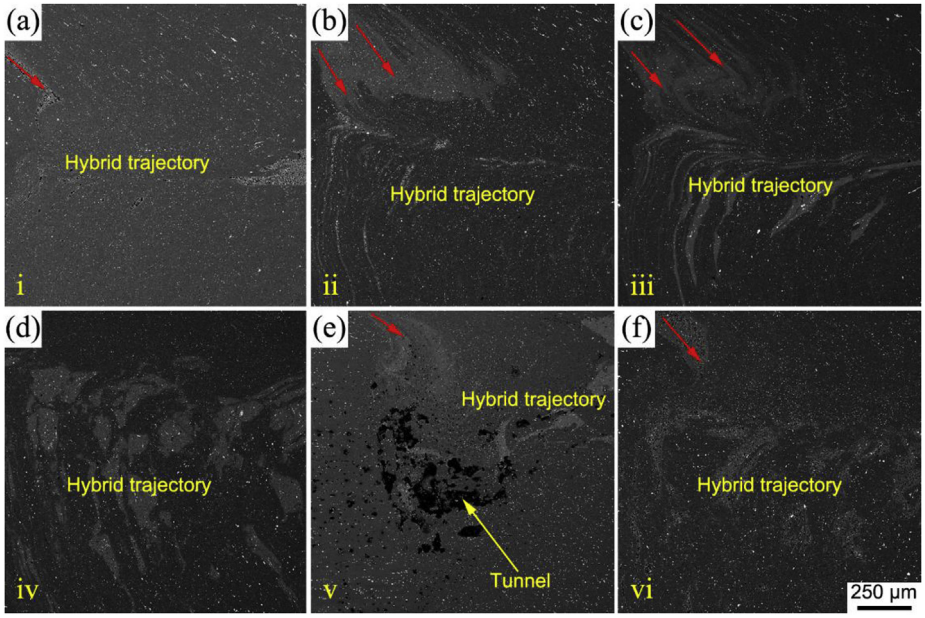

Fig. 5. BSE images of the C region in the six different combination types of the joints in Fig. 2.

BMs.

All the various welding combination types of the joints present different laminar flow or vortex patterns (Banded structure or onion ring patterns) present in the C region of the NZ in the joints. This indicates that materials are being transported from the RS to the AS in the C region (The direction of the white arrows in Fig. 6) and then pushed downward to the pin domain where the pushed materials (AA7075) and the original materials in this region (AA2024) are mixed and interspersed with each other. Finally, the complex combinations of flow patterns involving torsional and swirl motions are formed, which means flow direction of the materials in C region is from the RS to the AS. Besides, it can be observed from Figs. 5 and 6 that the materials from the shoulder domain near the AS flow towards the pin domain (The direction of the red arrows in Figs. 5 and 6) and material mixing takes place in the pin domain (Fig. 3). The tunnel defects present in the C region of the v joint, which indicates that less heat produced by the combination type of the 45°‖RD causes lower degree of plasticization and then results in insufficient mixing of materials.

EDS mapping was executed for the H, I and J regions in the NZ of the iii joint in Fig. 7. As displayed in Fig. 8, the distribution of Zn, Mg and Cu elements are obvious. The three regions (H, I and J) exhibit district material mixing, in which H and I regions present obvious stratified distribution (Fig. 8a and b), while the mixing of materials in J region shows more uniform distribution (Fig. 8c). The region H is located in the transition zone between the shoulder domain and the pin domain, which consists of the two BMs. The AA7075 BM in H region derives from two ways. One is that the AA7075 BM on the RS (Shoulder domain) is squeezed to the AS to form flow arm and then pushed down to the H region (Fig. 4, the direction of the red arrows in Figs. 5 and 6). The other is that the AA7075 BM on the RS (Shoulder domain) is extruded directly into the H region (The direction of the white arrows in Fig. 6). The J region located in the pin domain is mainly affected by the stirring pin. Part of the AA7075 BM in the H region is extruded into the pin domain, which intersects and mingles with the original AA2024 BM under the stir of the tool pin.

Fig. 9 shows the distribution of the second phases in the K (AS-NZ),

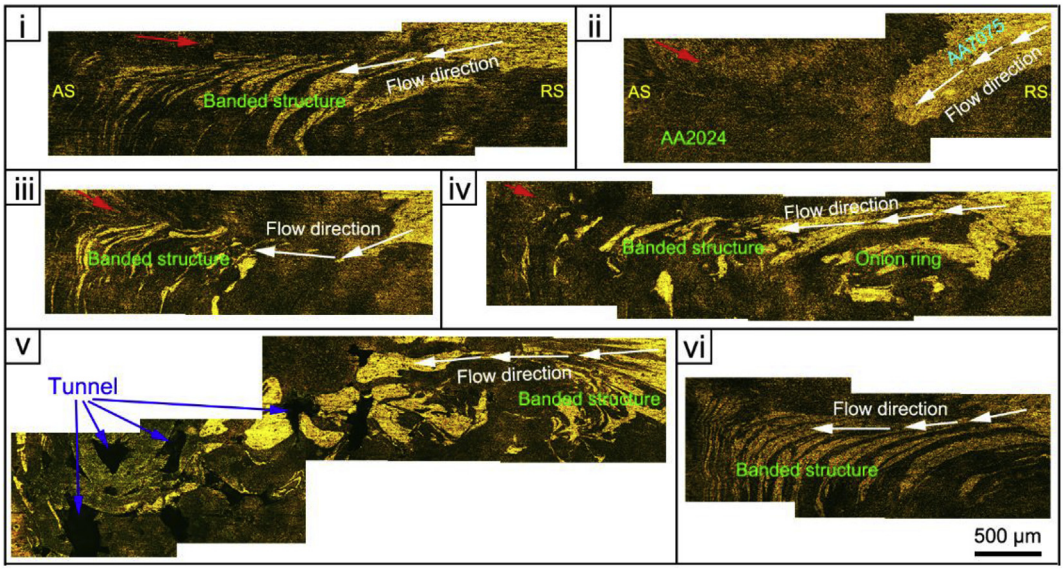

Fig. 6. Metallographic puzzles of the C region in the six joints in Fig. 2.

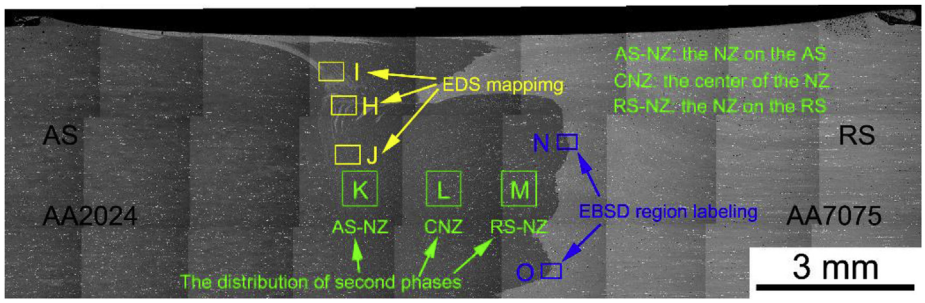

Fig. 7. BSE image puzzles of the iii joints in Fig. 2.

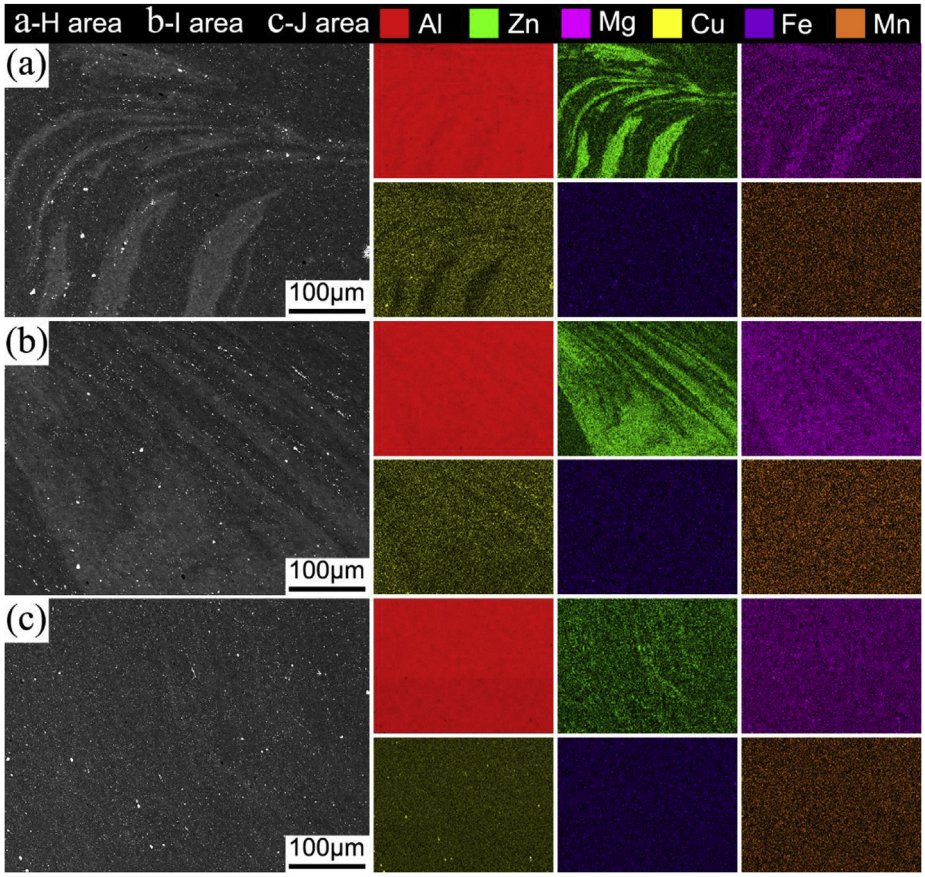

Fig. 8. EDS mapping (a) H area (b) I area and (c) J area in Fig. 7.

L (CNZ) and M (RS-NZ) regions in Fig. 7. The iii, iv and v joints are taken for examples. Apparently, the second phase distributions in the corresponding three regions of the three joints are similar. A large number of fine second phases appear in the AS-NZ and obvious flow trajectories of the second phases after crushed present in the CNZ. The number, density and size of the second phases in the RS-NZ are larger than that in the AS-NZ and CNZ, and part of the second phases are clustered together. The second phase distributions in the above three regions are related to the material flow during FSW. It is clearly observed from Figs. 3 and 9 that materials flow from the AS to the RS in the pin domain in the direction that is approximately counterclockwise, the flow path is curved. Under the agitation of the tool pin, the second phases are broken into fine particles in the AS-NZ and a linear trajectory (broken traces) is left in the CNZ. Finally, the broken second phases are pushed to the RS-NZ. The second phases are coarsened due to more heat being transported in the RS-NZ and aggregated together through the agitation of the tool pin.

Since there are differences in microstructure of the different positions in the NZ of the FSW joint, material flow in the NZ is asymmetrical about the rotational center axis [22]. According to the analysis of the above experimental results, the material flow diagram in the NZ is portrayed in Fig. 10. The specific material flow processes are as follows:

- In the tool shoulder domain, the extruded materials on the RS are pushed towards to the AS direction to form flow arm at the top surface of the AS (Figs. 3 and 4), and then flows downward. The materials on the AS are pushed to the RS and the downward direction under the extrusion and movement of tool shoulder. The material pushed from the AS to the RS is far more than that taking place in the opposite direction (Figs. 3 and 4).
- In the transition region between the tool shoulder domain and the tool pin domain, obvious flow patterns of mixed materials are formed (Fig. 8a). The materials in the transition region (AA7075) stems from two ways. One is that the materials on the RS (Shoulder domain) is squeezed to the AS to form flow arm and then pushed

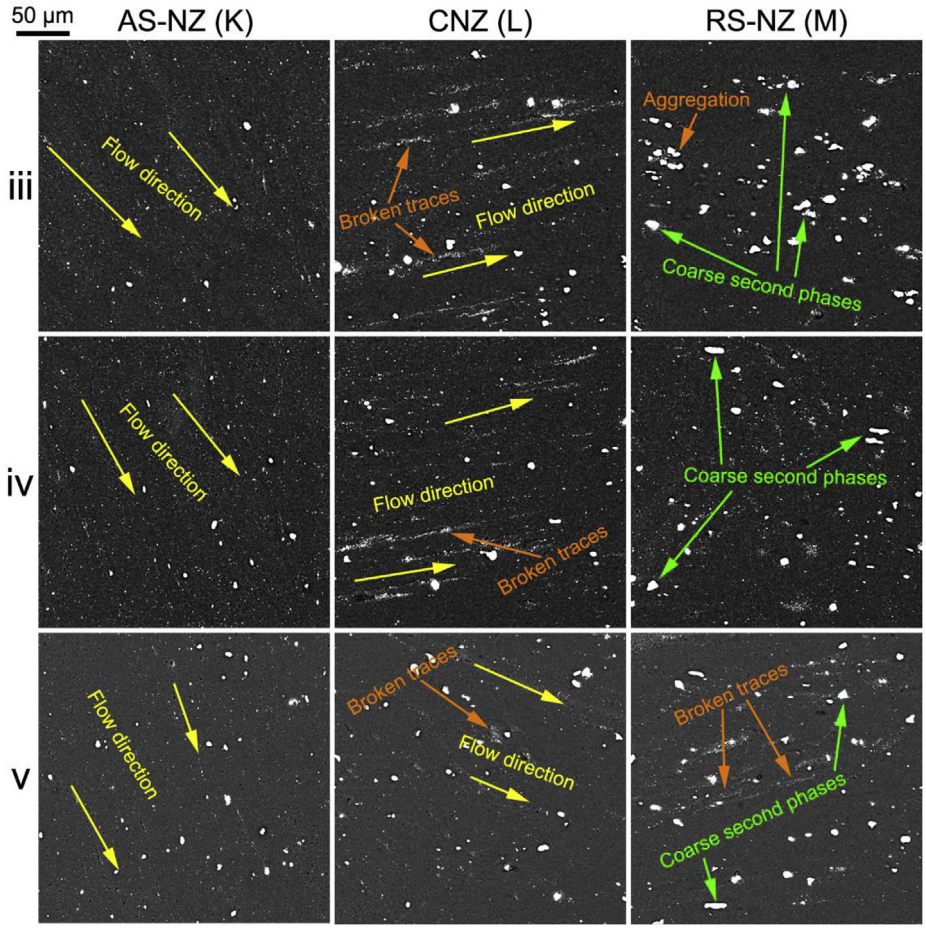

Fig. 9. BSE images of the second phase distributions of the K, L and M regions (Fig. 7) in the iii, iv and v joints.

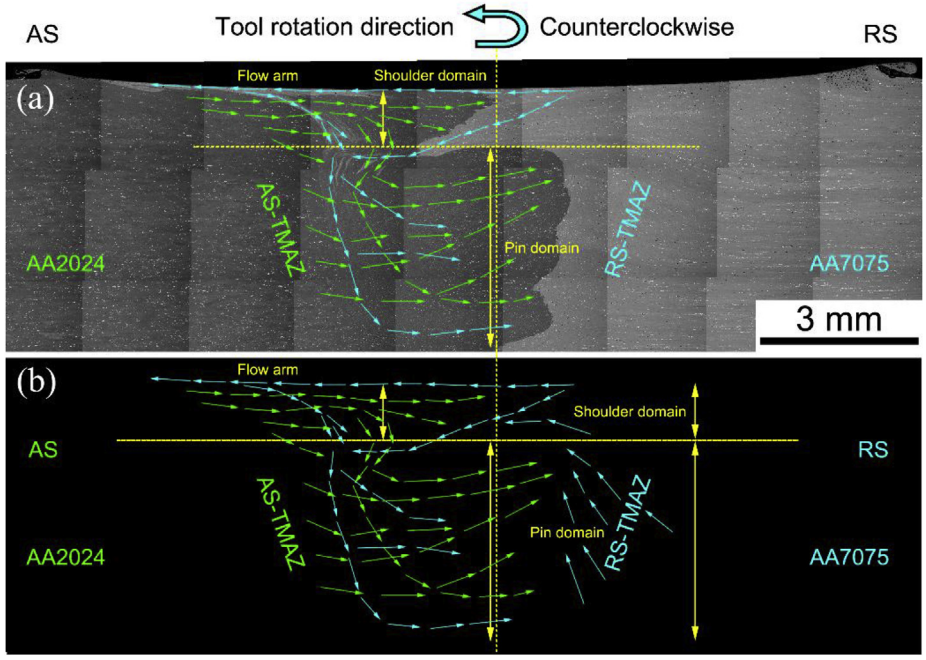

Fig. 10. Flow patterns (a) flow schematic diagram of the iii joint (b) summarization of material flow in the NZ.

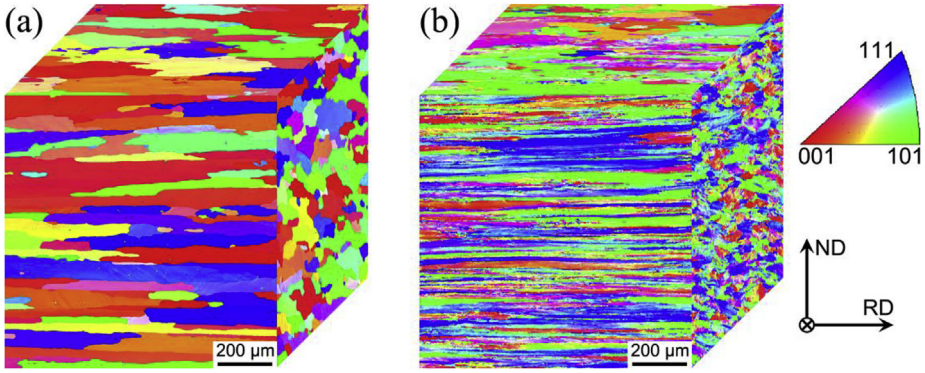

Fig. 11. Three dimensional IPF maps of the two BMs (a) AA2024 (b) AA7075.

down to the transition region (The A region in Fig. 4, the direction of the red arrows in Figs. 5 and 6). The other is that the materials on the RS (Shoulder domain) is extruded directly into the transition region (The direction of the white arrows in Fig. 6).

- In the tool pin domain, materials flow from the AS to the RS in a curvilinear way under the agitation of the tool pin, and the mixing of materials is relatively uniform (Fig. 8c). The second phases are broken into fine particles in the AS-NZ and a linear broken traces is left in the CNZ under the stir of the tool pin. The second phases are coarsened and aggregated together in the RS-NZ due to the heat from the flow process and the agitation of the tool pin (Fig. 9).

3.2. Microstructure

Fig. 11a and b displays the three dimensional IPF images of AA2024 and AA7075, respectively. The two BMs are composed of elongated grain structures along the rolling direction. The grains of the AA2024 are wider than that of the AA7075. Fig. 12 shows the optical micrographs of D and F regions of the joints in Fig. 2. Evidently, fine recrystallized grains are observed in the center (D region) and bottom (F region) of the six joints in comparison to the two BMs (Fig. 11). The heat and severe plastic deformation generated by the tool result in the recrystallization during FSW. The grain size in the center (D region) is higher than that at the bottom (F region), which is related to the temperature profile and heat dissipation in the NZ. Compared to the center region of the NZ, the peak temperature and the thermal cycle in the bottom region are lower and shorter because the bottom region is in contact with the backing plate and it is easy to lose heat. This is consistent with many other studies [13].

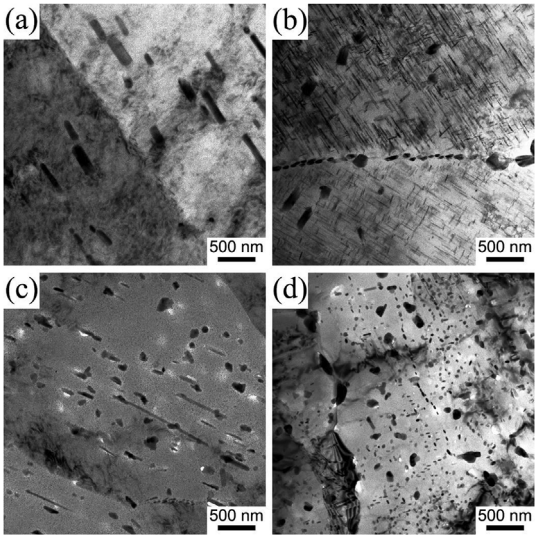

Fig. 13. TEM images of (a) AA2024 BM, (b) the HAZ on the AS of the iii joint, (c) AA7075 BM and (d) the HAZ on the RS of the iii joint.

Bright field TEM images of the two BMs and the HAZ on the AS and RS of the iii joint are shown in Fig. 13. The main strengthening precipitates of AA2024 alloy are needle-shaped Al_2Cu and rod-shaped Al_2CuMg precipitates [23]. These two kinds of phases are distributed

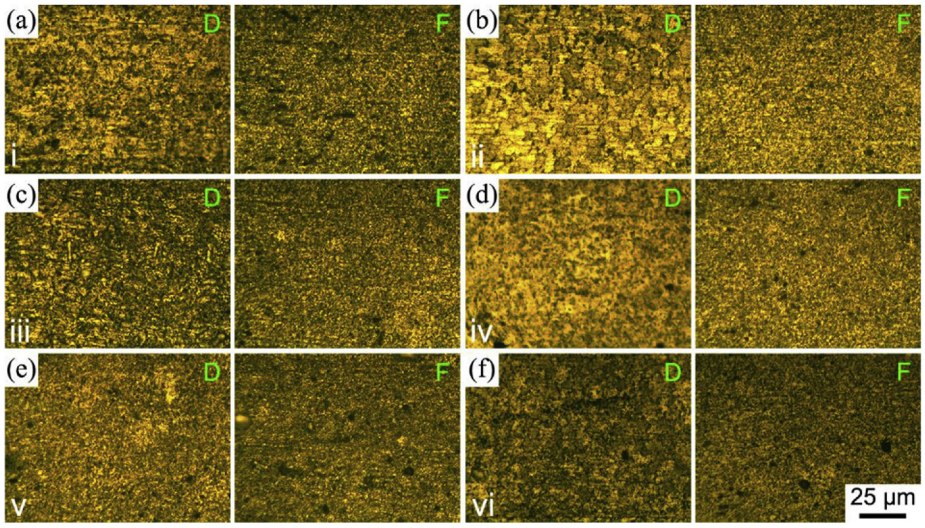

Fig. 12. Optical micrographs of D and F regions of the joints in Fig. 2.

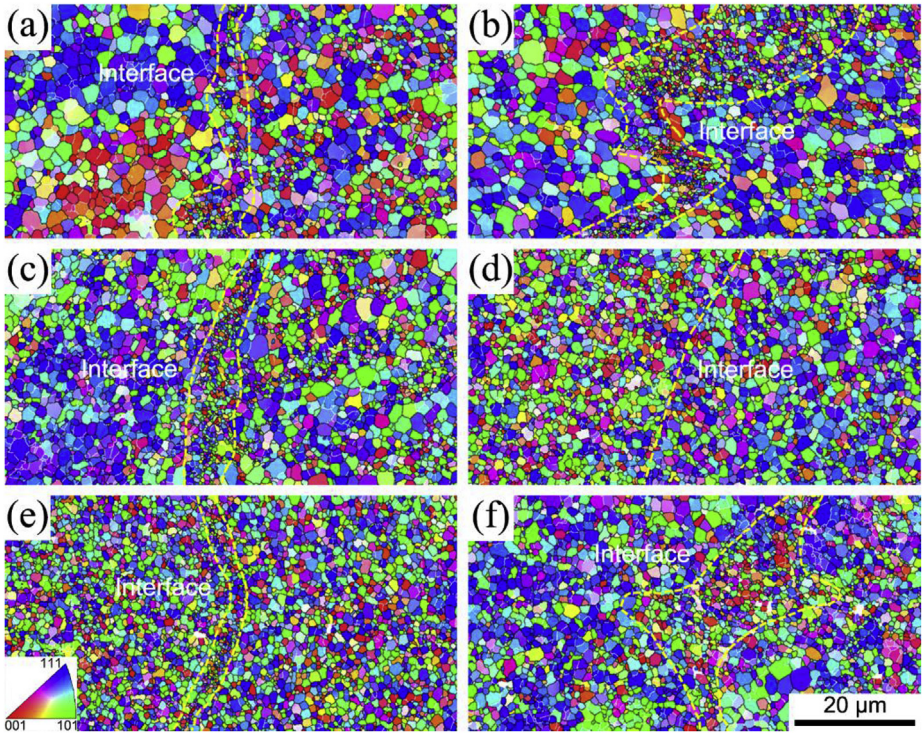

Fig. 14. IPF maps in the center interface zone (The N region in Fig. 7) of the six joints (a) i, (b) ii, (c) iii, (d) iv, (e) v and (f) vi.

and difficult to distinguish by reasons of the small size (Fig. 13a). The strengthening precipitates in the AA7075 alloy are well established as η′ ($Mg(ZnCuAl)_2$) and the grain boundary η ($MgZn^2$) precipitates [24]. Many intragranular and grain boundary precipitates are distributed in the TEM images (Fig. 13c). Fig. 13b and d are the TEM images of the HAZ on the AS and RS of the iii joint, respectively. The precipitate distribution is non-uniform with a duplex population. This distribution comprises of intragranular very small precipitates, while grain boundaries exhibit very coarse precipitates. The strengthening precipitates experience violent coarsening and partial dissolution because of the high peak temperature. The small precipitated phases present in the HAZ on the AS and RS as a result of the heterogeneous re-precipitation during cooling.

Grain structure in the center interface zone (The N region in Fig. 7) of the six joints is detailed in Fig. 14. Apparently, compared to the two BMs in Fig. 11, a large number of equiaxed grains exist in the center interface zone. This indicates that recrystallization occurs in the NZ, which can be attributed in violent plastic deformation and high heat input [25]. On the basis of the EBSD measurements, the average grain size in the center interface zone of all the joints are plotted as shown in Fig. 15. There is almost no significant change in the average grain size of the center interface zone in the six joints and the average value is around 2.4 μm, which indicates that the center interface zone of all the six joints undergoes the similar deformation and thermal cycle during FSW. However, bulk finer grains near the center interface region of the six joints are observed and the number of the fine grains is also various. Based on the partitioned statistics of EBSD maps (The grains smaller than 2 μm are retained), fine grain distribution maps partitioned from the matrix grains in Fig. 14 are summarized in Fig. 16. The number of fine grains in the center interface zone of the v joint is obviously higher than that of the other five joints (Fig. 17). This can be ascribed to the degree of material flow during FSW. The tunnel defect is generated in the NZ of the v joint (Figs. 5 and 6) due to insufficient material flow, meaning that the NZ of the v joint experiences less deformation and heat input. As a result, the broken grains near the center interface zone have no time to grow up, resulting in the residual of bulk fine grains.

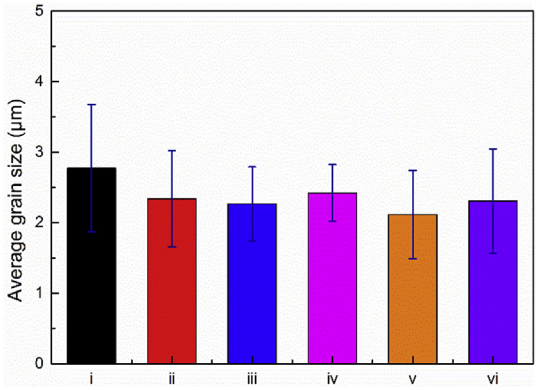

Fig. 15. Statistical results of average grain size in the center interface zone (Fig. 14) of the six joints.

It can be observed from the {111} PF in Fig. 16 that texture is formed in the fine grain zone near the center interface zone partitioned from the matrix grains (Fig. 14). Before analyzing the texture in the NZ, it is imperative to briefly debate the deformation during FSW. Simple shear texture exists in the NZ under the shear deformation resulting from the stir of the tool probe [26,27]. The shear texture is conventionally expressed in accordance with the crystallographic plane {hkl} and crystal direction < uvw > . The crystallographic plane {hkl} and direction < uvw > are aligned with the shear plane (probe surface) and shear direction (SD, probe surface tangent on the ND plane), respectively [28]. The primary shear deformation varies as a function of the location around the tool probe, i.e. for the center of the NZ. The SD and shear plane normal (SPN) are almost parallel to the TD and WD, respectively. Consequently, local texture analysis is carried out in the NZ so as to reveal the orientation feature of the joints. The {111} pole figure (PF) in Fig. 16 shows that the fine grain zone in the central interface zone of all the six joints has B and $\bar{B}$ texture components with a lower texture strength. The [29] PF and the corresponding orientation distribution function (ODF) maps of the entire center interface zone are displayed in Fig. 18. The center interface zone of all the six joint mainly

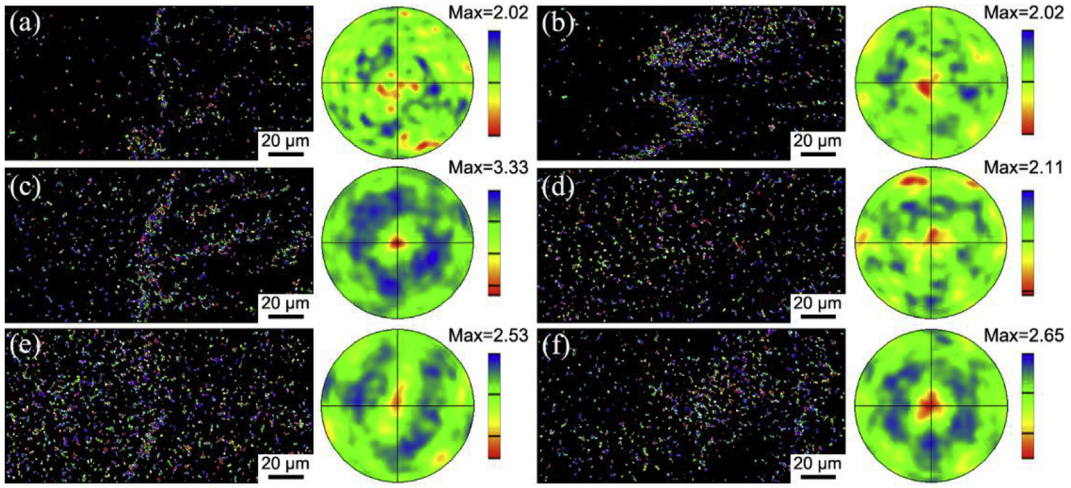

Fig. 16. Fine grain distribution maps partitioned from the matrix grains in Fig. 14 and the corresponding {111} PF (a) i, (b) ii, (c) iii, (d) iv, (e) v and (f) vi.

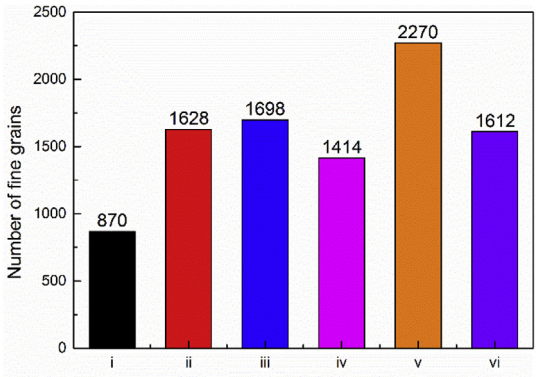

Fig. 17. Statistical results of the number of fine grains in the center interface zone (Fig. 14) of the six joints.

contains B and $\bar{B}$ texture components, while C texture component also presents in the center interface zone of the ii and v joints.

Fig. 19 shows the grain structure in the bottom interface zone (The O region in Fig. 7) of the six joints. It can be observed that bottom interface zone of the six joints contains bulk fine grains. After calculation and statistics, as shown in Fig. 20, the average grain size in the bottom interface zone of the v joints is about 1.09 μm, which is slightly lower than that of other joints (About 1.3 μm). This is because the v joint produces less heat input compared with other five joints and inadequate heat causes the broken grains grow too late. Besides, it is also found that many small angle grain boundaries exist in the grains near the interface line. That is, many sub-grains present in the grains near the interface line (The black arrows in Fig. 19). This is related to the agitation of the tool pin. The bottom area is mainly affected by the tip of the pin. The smaller diameter of the tip results in more limited acting area. In particular, material flow at the boundary is not violent and the grains are not sufficiently broken. Finally, parts of sub-grains are

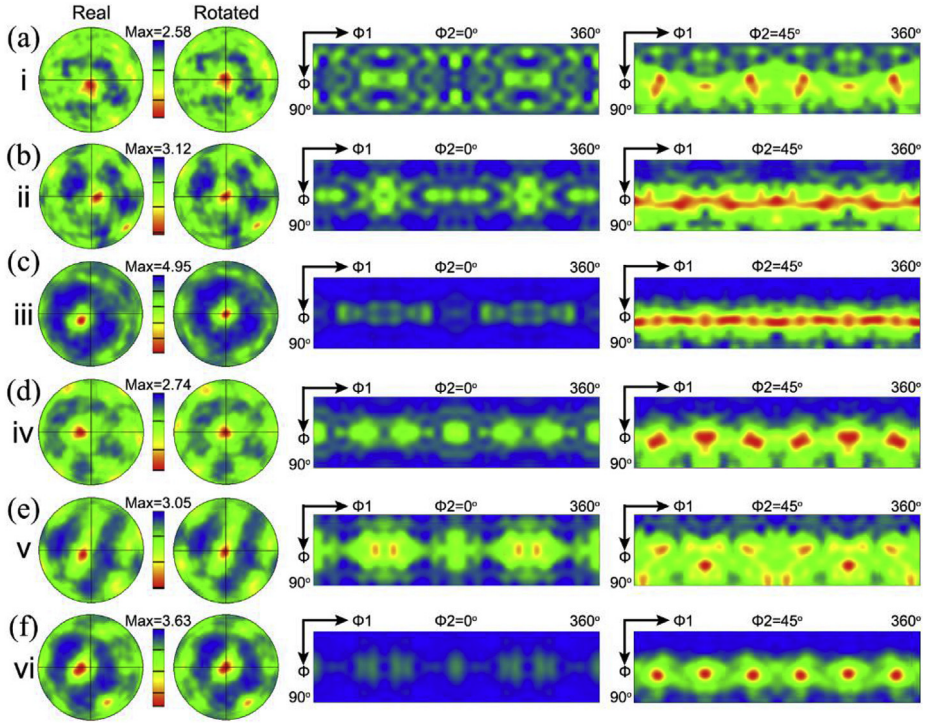

Fig. 18. PF and the corresponding ODF maps in the center interface zone (Fig. 14) of the six joints (a) i, (b) ii, (c) iii, (d) iv, (e) v and (f) vi.

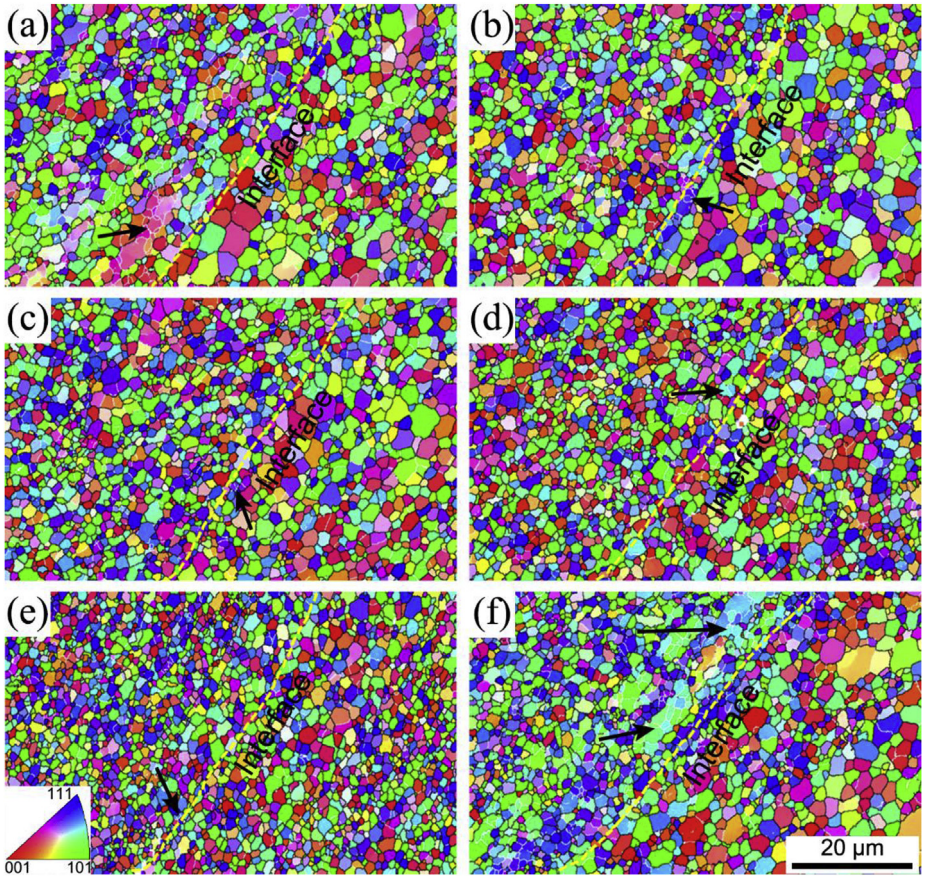

Fig. 19. IPF maps in the bottom interface zone (The O region in Fig. 7) of the six joints (a) i, (b) ii, (c) iii, (d) iv, (e) v and (f) vi.

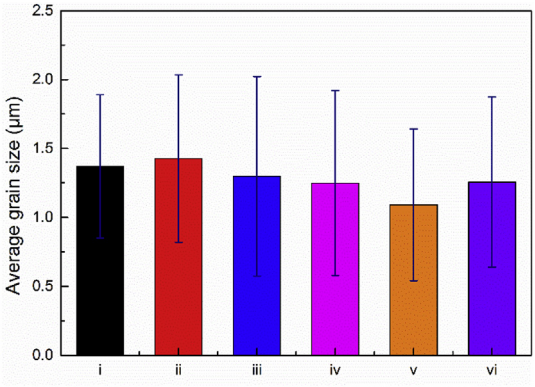

Fig. 20. Statistical results of average grain size in the bottom interface zone (Fig. 19) of the six joints.

retained near the bottom interface line.

Compared to the average grain size in the center interface zone (Fig. 15), a lower average grain size presents in the bottom interface zone. This further confirms the result of Fig. 12. During FSW, the temperature distribution is various at different positions in the NZ. Since the bottom region is in contact with the backing plate and that causes a lot of heat loss, the peak temperature and the thermal cycle in the center region is higher than those in the bottom region [30].

Fig. 21 displays the PF and the corresponding ODF maps in the bottom interface zone (Fig. 19) of the six joints. It is clearly observed that the bottom interface zone of all the six joints contains the same texture types. They are the A_1^* and A_2^* texture components and there is almost no significant change in the texture strength of all the joints. Shen et al. [31] clarified that the texture components are directly correlated with the magnitude of shear strain. In brief, A_1^* and A_2^* texture components generate at lower strains. As the strain is increased, C component is dominant at a shear strain of 10–16. When the strain continues to increase, B and $\bar{B}$ texture components are predominant at a minimum shear strain of 20 or higher. Accordingly, in this respect, the ii and v joint suffers larger strain compared with the i, iii, iv and vi joints in the center interface zone (Fig. 18). In the bottom, all the six joints experience the same smaller strain during FSW (Fig. 21). Moreover, it can be concluded that the center interface zone (Fig. 18) is subjected to larger shear strain than that in the bottom interface zone (Fig. 21).

3.3. Hardness test

Fig. 22 illustrates the micro-hardness profiles at the center line of thickness in the cross-section region of the six joints. The hardness distribution profiles of the six joints show the W shape. A lower hardness zone on both AS and RS are observed in the weld compared to their corresponding BMs. This is mainly due to the coarsening, dissolution and re-precipitation of strengthening precipitates (Fig. 13) caused by FSW thermal cycle [24]. The micro-hardness distribution is quite heterogeneous, particularly in the NZ consisting of AA 2024 and AA7075 BMs (Fig. 3).

It should be noted that the above single hardness profile could not identify the fracture path of the FSW joints. In order to accurately analyze the fracture behavior of the joints, the hardness maps are portrayed in Fig. 23. It can be found that all the six joints show the asymmetric hardness distribution profiles due to the asymmetrical heat generation and material flow caused by the FSW tool, which is typical for the dissimilar FSW joint. Visibly, the softening area of the i and ii joints is in the NZ on the AS. The softening area of the iii, iv and vi

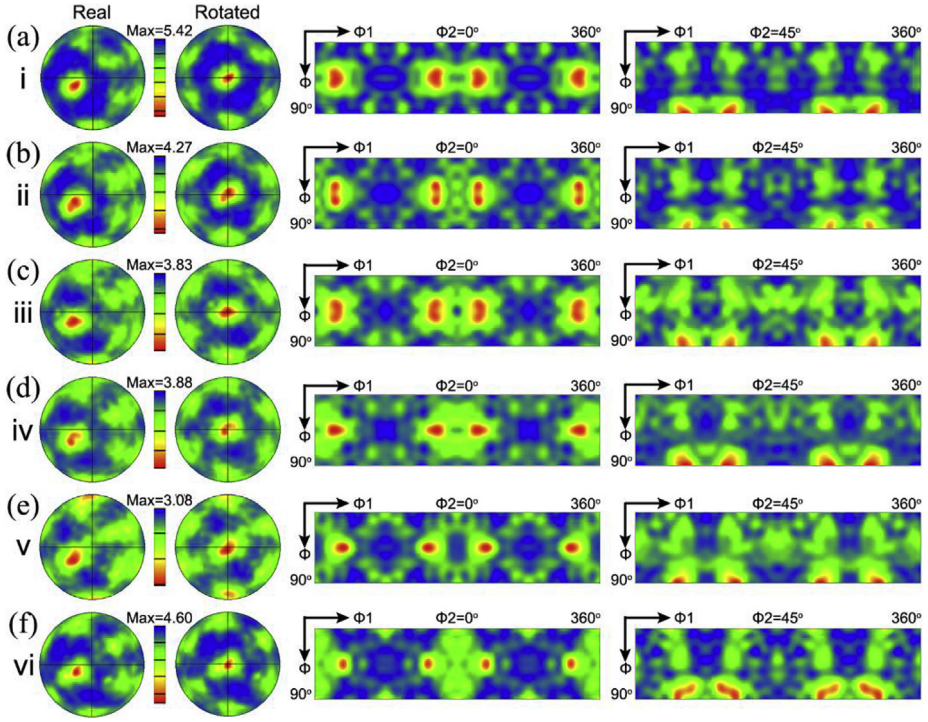

Fig. 21. PF and the corresponding ODF maps in the bottom interface zone (Fig. 19) of the six joints (a) i, (b) ii, (c) iii, (d) iv, (e) v and (f) vi.

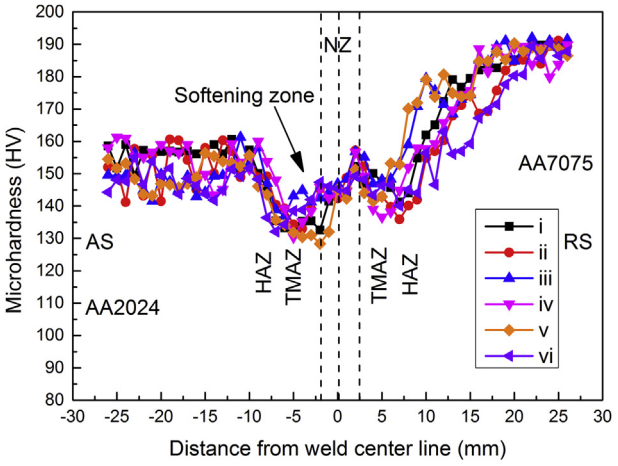

Fig. 22. Micro-hardness profiles in the center line of the cross-section thickness of the six joints.

joints is in the HAZ on the AS. It is considered that the iii, iv and vi joints produce higher heat input and then lead to higher softening degree of the HAZ, while the i and ii joints produce less heat and the softening degree of the HAZ is lower. For the v joint, the softening area is located where the tunnel occurs (Fig. 3). Consequently, the hardness maps can be helpful to analyze the fracture behavior of the joints.

3.4. Tensile properties

Fig. 24a and b are the tensile engineering stress-strain cures and the tensile data results of the joints with the six types of weld combinations, respectively. It is obvious that the elastic deformation stages of all joints are almost overlapped, but there is a distinct difference in the plastic deformation stages. In order to evaluate that the effect of the different weld combinations on tensile properties of the joints, the values of yield strength (YS), ultimate tensile strength (UTS), tensile elongation (TE) are re-plotted in Fig. 24b. Clearly, the tensile property of the v joint (YS-143.6 MPa, UTS-150.2 MPa, TE-1.36%) is the worst due to the insufficient plasticization of the materials and low material flow (Figs. 2 and 6). The iii joint with maximum tensile strength (YS- 323.8 MPa, UTS-445.6 MPa) is acquired as a result of suitable heat input and high material flow efficiency. Except for the iii and v joint, the other joints have the similar YS and UTS. In addition, the TE of the iii joint is slightly lower than that of the i, iii and vi joints. The superior mechanical properties of the iii joint indicates that this welding combination type produces a more sufficient material mixing and more suitable heat input. This is because low heat input leads to poor plastic flow and formation of defects in the weld zone. These defects are the location of crack initiation during tensile tests and hence contribute to low tensile properties. Conversely, high heat input definitely results in coarsening or dissolution of strengthening precipitates at the welded zone, Thus, the tensile strength of the joints is also lower.

The microstructural evolution occurs during FSW, accompanied by a significant change of residual stress. Both of them have a district effect on the mechanical properties of the joints [32]. Tensile and compressive residual stress can be generated inside the weld. The maximum tensile stress is located in the HAZ, while the minimum compressive stress can be obtained on the AS just beyond the weld zone [33]. This variation in residual stress is important to analyze the performance of the joints. During FSW, the formation of residual stress is attributed to the localized heat input and significant temperature gradient along the width of the welded plates [32]. Thus, we can summarize that the distribution of residual stress in the weld zone with different welding combinations is different, which is prone to affect the mechanical properties of the joints. Since this work mainly focuses on the microstructure and mechanical properties of the dissimilar FSW joints, the influence of residual stresses has not been considered.

3.5. Fracture behavior

The fracture locations of joints produced with different types of weld combinations are demonstrated in Fig. 25. Three fracture locations can be identified and represented as Mode FLI, Mode FLII and Mode FLIII. In mode LFI, the failure of the i and ii joints occurs in the

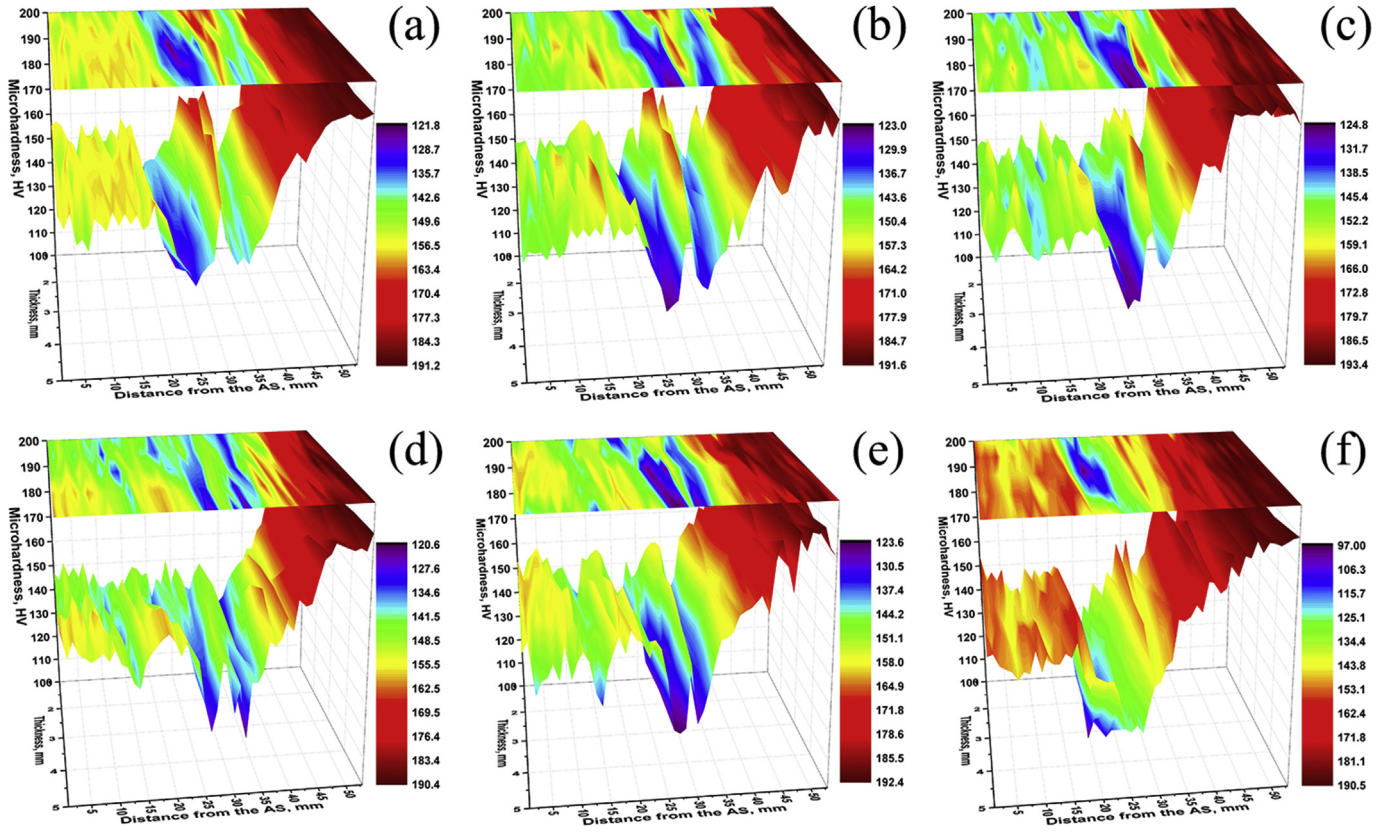

Fig. 23. Micro-hardness counter maps across the cross-section regions of the six joints.

NZ (Fig. 25a and b). In Mode LFII, the iii, iv and vi joints fracture in the HAZ (Fig. 25c, d and f). The minimum hardness is located in the HAZ, which is usually the main fracture location of the FSW aluminum alloy joints [13]. In Mode LFIII, failure occurs where tunnel defect forms (Fig. 25e).

Fig. 26 shows the fractured morphologies corresponding the above three modes using the three joints (Mode FLI – the i joint, Mode FLII – the iii joint and Mode FLIII – the v joint.). For Mode FLI, the fracture surface presents curved band structure (Fig. 26a). The formation of banded structure can be related to the material flow during FSW (Fig. 3). While for Mode FLII, the fracture surface is characterized by many large and shallow dimples that are interspersed with smooth cleavage surfaces. The initial rolling direction of the plates presents in the fracture surface (Fig. 26d and e) since the fracture occurs in the HAZ on the AS (Fig. 25c). It can be observed from Fig. 24 that the TE of the iii joint is lower than that of the i joint, due to the fact that the main fracture mode of the i joint is ductile fracture while that of the iii joint is ductile-brittle fracture. This change of fracture mode can be mainly attributed to the transformation of fracture location from the NZ to the HAZ on the AS (Fig. 25), due to the microstructural evolution in the weld zone of the joints resulting from different types of welding combinations. Many small and deep dimples are found in the locally magnified view (Fig. 26 b and c), which can be determined as a ductile fracture. The ductile-brittle fracture is characterized by many large and shallow dimples that are interspersed with smooth cleavage surfaces. Additionally, some particles can be found inside the dimples through BSE images (marked by A and B arrows in Fig. 26). These particles are the location of the fracture initiation, which could provide suitable conditions for crack nucleation. It is well known that overload results in fracture of the dimple rupture mode and the failure is controlled by coalescence of microvoids, which may nucleate near the second phase particles, inclusions and so on [34]. Hence, during the tensile test, the microvoids grow and merge to form a continuous fracture. Accordingly, the shallower dimples in the iii joint result from more severe precipitate

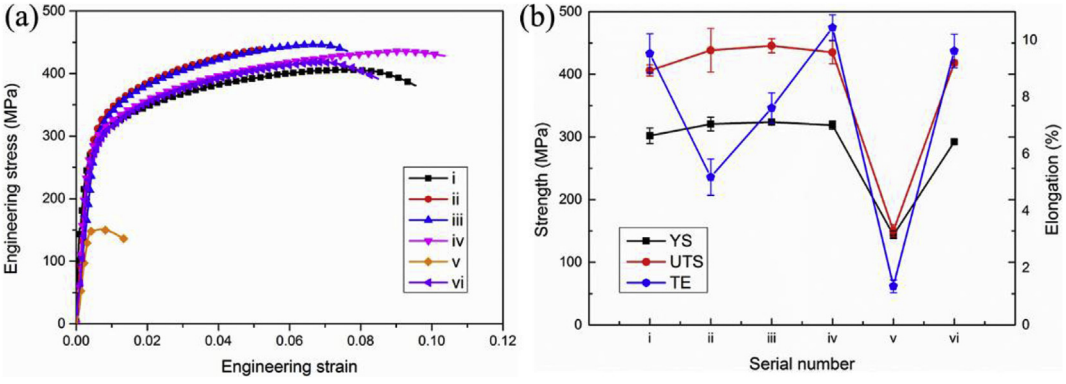

Fig. 24. (a) Engineering stress-strain cures and (b) tensile stress and elongation of joints with the six types of weld combinations.

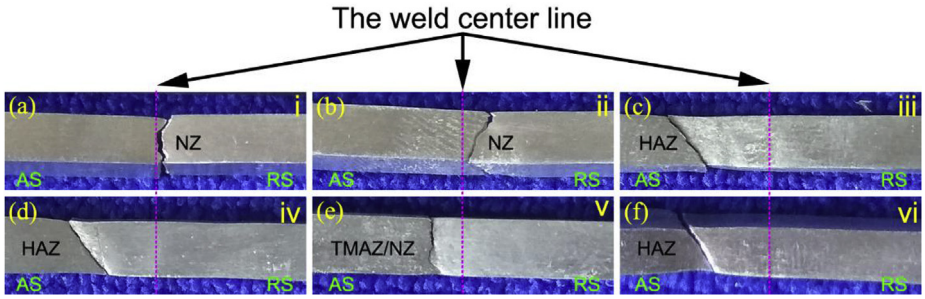

Fig. 25. Fracture locations of the six combination types of joints.

coarsening occurring during FSW (Figs. 13b and 26f). For Mode FLIII, some voids and cambium lamellar areas are observed from Fig. 26g–i. This is because the fracture location of the v joint is located in the area where the tunnel defect (marked by C arrow in Fig. 26) is generated due to the insufficient material flow (Figs. 5 and 6).

4. Conclusion

In this work, six different types of combinations with respect to the BMs rolling direction were subjected to the dissimilar FSW of AA2024-T351 and AA7075-T651. The effect of joining material direction on the microstructure and mechanical properties of the dissimilar FSW joints was systematically investigated. The following conclusions could be derived:

- The tunnel defect is generated in the 45°‖RD type of weld combination joint, while the other five types of combinations are successfully welded.
- Material mixed flow mainly occurs in the following three regions: the tool shoulder domain, the tool pin domain and the transition region between the shoulder domain and the pin domain.
- In the tool shoulder domain, the material pushed from the AS to the RS is far more than that taking place in the opposite direction. The materials on the RS are extruded towards to the AS direction to form flow arm at the top surface of the AS, and then flows towards down. The materials on the AS are pushed to the RS and the NZ direction under the extrusion and movement of the tool shoulder.
- The materials of the RS in the transition region derives from two approaches in the shoulder domain. One is that the materials on the RS is squeezed to the AS to form flow arm and then pushed down to the transition region. The other is that the materials on the RS of the shoulder domain is extruded directly into the transition region.

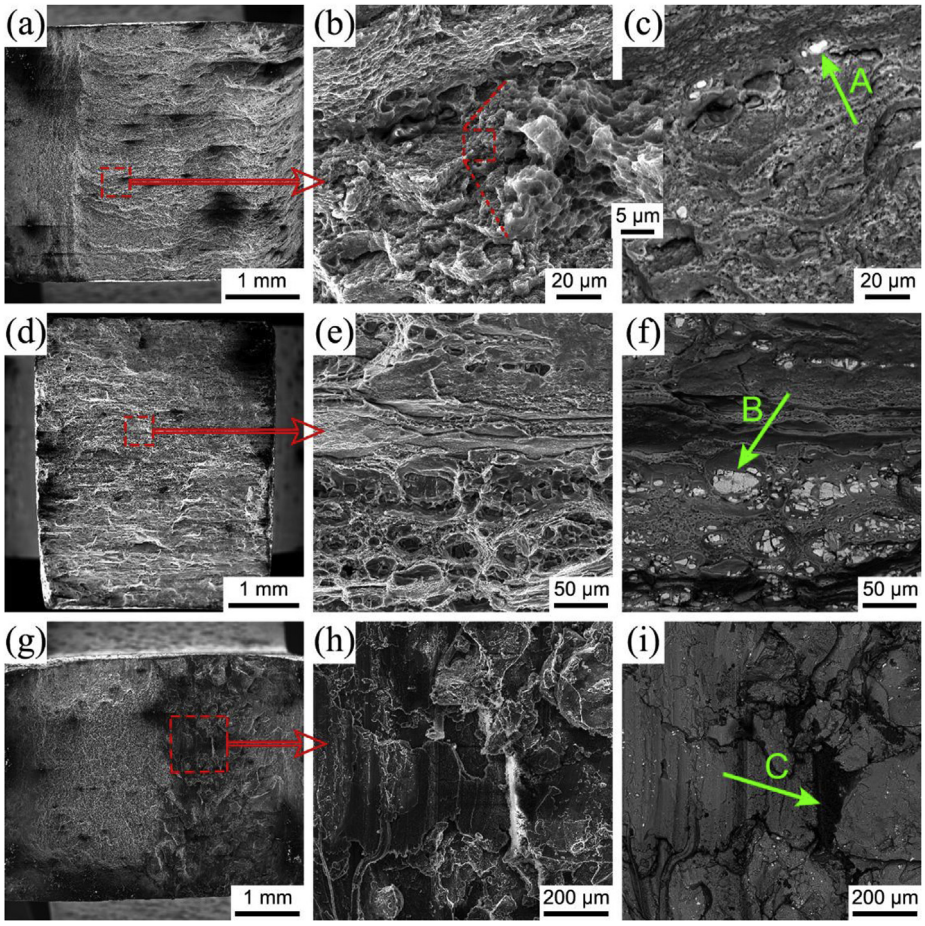

Fig. 26. Fractured surface of the tensile samples under SEM for (a–c) the i joint (d–f) the iii joint (g–i) the v joint.

- Materials flow from the AS to the RS in a curvilinear way under the agitation of the tool pin in the pin domain. The second phases are broken into fine particles in the AS-NZ and a linear broken traces is left in the CNZ under the stir of the tool pin. The second phases are coarsened and aggregated together in the RS-NZ.
- The average grain size in the center zone of the NZ is higher than that in the bottom zone. The fine grain zone near the central interface line of all the six joints has B and $\overline{B}$ texture. The central interface zone of all the six joint mainly contains B and $\overline{B}$ texture components, while B, $\overline{B}$ and C are the major texture components in the central interface zone of the ii and v joints. The bottom interface zone of all the six joints contains the same A_1^* and A_2^* texture components.
- The maximum tensile strength is acquired as 445.6 MPa for the RD∥TD joint as a result of suitable heat input and sufficient material flow, while the minimum tensile strength is obtained as 150.2 MPa for the 45°∥RD joint due to the formation of tunnel defect resulting from the insufficient heat input.
- The fracture location of the 45°∥RD joint is where the tunnel defect forms. The other five joints fracture in the softening zone of the hardness value.

Acknowledgments

The authors would like to acknowledge the “Fundamental Research Funds for the Central Universities” (106112015CDJXY130003, 106112018CDXYCL0018, 106112015CDJXZ138803, “National Natural Science Foundation of China” (51,421,001) and “Open Science and Technology Cooperation Project of Henan Province” (182106000024) for financial support and Electron Microscopy Center of Chongqing University for providing SEM and TEM test channel.

References

[1] T. Dursun, C. Soutis, Recent developments in advanced aircraft aluminium alloys, Mater. Des. 56 (2014) 862–871.
[2] E. Cetkin, Y. Çelik, S. Temiz, Microstructure and mechanical properties of AA7075/AA5182 jointed by FSW, J. Mater. Process. Technol. 268 (2019) 107–116.
[3] C. Zhang, G. Huang, Y. Cao, Y. Zhu, Q. Liu, On the microstructure and mechanical properties of similar and dissimilar AA7075 and AA2024 friction stir welding joints: effect of rotational speed, J. Manuf. Process. 37 (2019) 470–487.
[4] G. Çam, G. İpekoğlu, Recent developments in joining of aluminum alloys, Int. J. Adv. Manuf. Technol. 91 (2017) 1851–1866.
[5] N. Kashaev, V. Ventzke, G. Çam, Prospects of laser beam welding and friction stir welding processes for aluminum airframe structural applications, J. Manuf. Process. 36 (2018) 571–600.
[6] R. Nandan, T. DebRoy, H. Bhadeshia, Recent advances in friction-stir welding–-process, weldment structure and properties, Prog. Mater. Sci. 53 (2008) 980–1023.
[7] P. Threadgill, A. Leonard, H. Shercliff, P. Withers, Friction stir welding of aluminium alloys, Int. Mater. Rev. 54 (2009) 49–93.
[8] R.S. Mishra, Z. Ma, Friction stir welding and processing, Math. Sci. Eng. R 50 (2005) 1–78.
[9] C. Zhang, G. Huang, Y. Cao, X. Wu, X. Huang, Q. Liu, Optimization of tensile and corrosion properties of dissimilar friction stir welded AA2024-7075 joints, J. Mater. Eng. Perform. 28 (2019) 183–199.
[10] G. Çam, Friction stir welded structural materials: beyond Al-alloys, Int. Mater. Rev. 56 (2011) 1–48.
[11] D.M. Neto, P. Neto, Numerical modeling of friction stir welding process: a literature review, Int. J. Adv. Manuf. Technol. 65 (2013) 115–126.
[12] Z. Ma, A. Feng, D. Chen, J. Shen, Recent advances in friction stir welding/processing of aluminum alloys: microstructural evolution and mechanical properties, Crit. Rev. Solid State 43 (2018) 269–333.
[13] G. Cam, S. Mistikoglu, Recent developments in friction stir welding of Al-alloys, J. Mater. Eng. Perform. 23 (2014) 1936–1953.
[14] S.-K. Park, S.-T. Hong, J.-H. Park, K.-Y. Park, Y.-J. Kwon, H.-J. Son, Effect of material locations on properties of friction stir welding joints of dissimilar aluminium alloys, Sci. Technol. Weld. Join. 15 (2010) 331–336.
[15] P. Cavaliere, R. Nobile, F. Panella, A. Squillace, Mechanical and microstructural behaviour of 2024–7075 aluminium alloy sheets joined by friction stir welding, Int. J. Mach. Tool Manuf. 46 (2006) 588–594.
[16] R. Palanivel, P.K. Mathews, N. Murugan, I. Dinaharan, Effect of tool rotational speed and pin profile on microstructure and tensile strength of dissimilar friction stir welded AA5083-H111 and AA6351-T6 aluminum alloys, Mater. Des. 40 (2012) 7–16.
[17] D. Kim, W. Lee, J. Kim, C. Kim, K. Chung, Formability evaluation of friction stir welded 6111-T4 sheet with respect to joining material direction, Int. J. Mech. Sci. 52 (2010) 612–625.
[18] A. Barbini, J. Carstensen, J. dos Santos, Influence of alloys position, rolling and welding directions on properties of AA2024/AA7050 dissimilar butt weld obtained by friction stir welding, Metals 8 (2018) 202.
[19] N.Z. Khan, A.N. Siddiquee, Z.A. Khan, S.K. Shihab, Investigations on tunneling and kissing bond defects in FSW joints for dissimilar aluminum alloys, J. Alloy. Comp. 648 (2015) 360–367.
[20] A. Tongne, C. Desrayaud, M. Jahazi, E. Feulvarch, On material flow in friction stir welded Al alloys, J. Mater. Process. Technol. 239 (2017) 284–296.
[21] P. Li, G. You, H. Wen, W. Guo, X. Tong, S. Li, Friction stir welding between the high-pressure die casting of AZ91 magnesium alloy and A383 aluminum alloy, J. Mater. Process. Technol. 264 (2019) 55–63.
[22] T. Seidel, A.P. Reynolds, Visualization of the material flow in AA2195 friction-stir welds using a marker insert technique, Metall. Mater. Trans. A 32 (2001) 2879–2884.
[23] C. Genevois, A. Deschamps, A. Denquin, B. Doisneau-Cottignies, Quantitative investigation of precipitation and mechanical behaviour for AA2024 friction stir welds, Acta Mater. 53 (2005) 2447–2458.
[24] J.-Q. Su, T. Nelson, R. Mishra, M. Mahoney, Microstructural investigation of friction stir welded 7050-T651 aluminium, Acta Mater. 51 (2003) 713–729.
[25] M. Ahmed, S. Ataya, M.E.-S. Seleman, H. Ammar, E. Ahmed, Friction stir welding of similar and dissimilar AA7075 and AA5083, J. Mater. Process. Technol. 242 (2017) 77–91.
[26] T. Wang, Y. Zou, K. Matsuda, Micro-structure and micro-textural studies of friction stir welded AA6061-T6 subjected to different rotation speeds, Mater. Des. 90 (2016) 13–21.
[27] R. Fonda, A. Reynolds, C. Feng, K. Knipling, D. Rowenhorst, Material flow in friction stir welds, Metall. Mater. Trans. A 44 (2013) 337–344.
[28] R. Fonda, J. Bingert, Texture variations in an aluminum friction stir weld, Scr. Mater. 57 (2007) 1052–1055.
[29] C. Escrivà-Cerdán, E. Blasco-Tamarit, D.M. García-García, J. García-Antón, R. Akid, J. Walton, Effect of temperature on passive film formation of UNS N08031 Cr–Ni alloy in phosphoric acid contaminated with different aggressive anions, Electrochim. Acta 111 (2013) 552–561.
[30] N. Martinez, N. Kumar, R. Mishra, K. Doherty, Microstructural variation due to heat gradient of a thick friction stir welded aluminum 7449 alloy, J. Alloy. Comp. 713 (2017) 51–63.
[31] J. Shen, F. Wang, U.F. Suhuddin, S. Hu, W. Li, J.F. Dos Santos, Crystallographic texture in bobbin tool friction-stir-welded aluminum, Metall. Mater. Trans. A 46 (2015) 2809–2813.
[32] A.L. Biro, B.F. Chenelle, D.A. Lados, Processing, microstructure, and residual stress effects on strength and fatigue crack growth properties in friction stir welding: a review, Metall. Mater. Trans. B 43 (2012) 1622–1637.
[33] L. Fratini, B. Zuccarello, An analysis of through-thickness residual stresses in aluminium FSW butt joints, Int. J. Mach. Tool Manuf. 46 (2006) 611–619.
[34] J. Guo, H. Chen, C. Sun, G. Bi, Z. Sun, J. Wei, Friction stir welding of dissimilar materials between AA6061 and AA7075 Al alloys effects of process parameters, Mater. Des. 56 (2014) 185–192.